Examining the Links Between the Quasi-Biennial Oscillation, the Madden-Julian Oscillation, and the El Niño-Southern Oscillation Using Linear Inverse Modeling

Juliana Harr

A Thesis submitted in partial fulfillment of

the requirements for the degree of

Master of Science

(Atmospheric and Oceanic Sciences)

at the

UNIVERSITY OF WISCONSIN-MADISON

August 2023

Abstract

The Quasi-Biennial Oscillation (QBO) describes a pattern of downward-propagating stratospheric winds which alternate directions between easterly and westerly. Many recent studies have explored the possible links between the QBO and other climate phenomena, such as the Madden-Julian Oscillation (MJO) and the El Niño-Southern Oscillation (ENSO). Due to a lot of overlap between MJO and ENSO signals, it often proves difficult to isolate the individual effects of these phenomena, and their relationship to the QBO. To complicate the matter further, studies are restricted by the limited amount of data from the historical record. This study incorporates the use of linear inverse modeling (LIM) to empirically derive a dynamical model based on observed statistics. By using a linear inverse model, a number of techniques can be employed to further examine these complex relationships. One such technique is filtering, in which dynamical modes of variability can be isolated from the data, allowing for separate investigations of these processes. Another method involves the use of the LIM as a free-running climate model, where statistics from the existing record of data are used to generate thousands of years of new data points. This is particularly useful given the obstacle of having limited data from the historical record. These LIM-based techniques are utilized in order to assess the QBO-MJO-ENSO relationships and the physical processes behind them.

Acknowledgements

Contents

List of Figures

List of Tables

Chapter 1

Introduction

1.1 The Quasi-Biennial Oscillation

The Quasi-Biennial Oscillation (QBO) describes an alternating pattern of downward-propagating winds in the tropical stratosphere. With a period of approximately 28 months, these zonal winds change directions between easterly and westerly (Baldwin et al. 2001). First theories of the QBO can be traced back to the volcanic eruption of Krakatau in 1883, in which debris from the eruption had been carried across the globe by upper-level winds in a matter of weeks (Maruyama 1997). However, a formal discovery of the QBO was not until approximately 1960. R.J. Reed and R.A. Ebdon are largely accredited with this discovery, on behalf of their research assessing the downward propagation of stratospheric winds and length of QBO periods (Reed et al. 1961; Ebdon 1960).

As QBO winds propagate downward, they begin to lose some of their amplitude before finally dissipating at the tropopause (Baldwin et al. 2001). Because of this reduction in amplitude, a driving force is needed in order to sustain QBO processes (Wallace and Holton 1968). Large-scale atmospheric waves are thought to be the source behind QBO maintenance and initiation. Vertically-propagating gravity waves are found to be a major contributor to the QBO's downward motions, based on analysis of momentum fluxes and background flow (Lindzen and Holton 1968). Equatorial Kelvin waves are also a point of interest, due to their upward flux of westerly momentum leading to QBO westerlies (Wallace and Kousky 1968). Another solution consisting of mixed Rossby-gravity waves can produce a net easterly acceleration needed for the easterly phase of the QBO (Bretherton 1969).
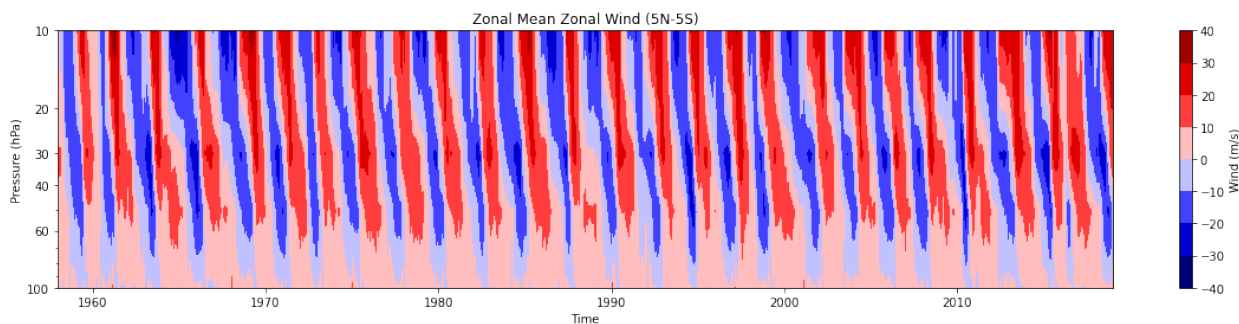

FIGURE 1: Pressure vs. time plot of zonally-averaged equatorial zonal wind anomalies. EQBO is represented by the negative blue anomalies while WQBO is plotted as positive red anomalies.

Time-height plots of equatorial winds are a useful way to visualize QBO activity, as shown in Figure 1. This figure depicts zonally-averaged winds descending over time, as shown by the slant in the wind anomalies. Alternating easterly (blue) and westerly (red) phases are represented by the colors. The QBO's easterly phase, referred to as EQBO, tends to be stronger in amplitude than the westerly phase. A possible explanation for this is that EQBO is associated with an upward advection of momentum that effectively traps easterly winds in the stratosphere and prevents them from losing too much of their amplitude as they propagate downward (Baldwin 2001). On the other hand, the westerly phase of the QBO (WQBO) is linked to a downward advection of momentum, which results in this phase having a faster and more regular propagation.

1.2 The Madden-Julian Oscillation

Since its discovery in the early 1970s, the Madden-Julian Oscillation (MJO) has been a primary part of tropical atmospheric research. Roland Madden and Paul Julian first documented MJO activity through radiosonde analysis of zonal wind and surface pressure in the tropical Pacific (Madden and Julian 1971,1972). Based on their findings, the MJO came to be understood as a planetary-scale system that propagates eastward and is characterized by changes in circulation and convection (Zhang 2005). The MJO is considered to be the leading mode of intraseasonal variability in the tropics, defined by its 30- to 90-day period. A typical MJO event consists of a region of enhanced convection and precipitation, followed and preceded by regions of suppressed convection and precipitation. The whole system moves eastward at a phase speed of approximately 5 m/s, from the Indian Ocean to the western and central Pacific Ocean (Zhang 2005).

The MJO extends all throughout the troposphere, with westerly winds to the west of the convective center at the surface, and easterly winds to the east. At the top of the troposphere, these winds change directions. This coupling between convection and circulation plays a critical role in MJO dynamics. One way of examining this relationship is through the role of water vapor. MJO circulation can induce fluctuations in water vapor, where a moistening of the atmosphere supports the development of deep convection (Tompkins 2001). Atmosphere-ocean coupling is additionally an important part of MJO initiation and maintenance. Convection tends to favor warm sea surface temperature conditions, where air-sea interactions can provide energy for MJO cycles (Krishnamurti et al. 1988).

The MJO has been known to modulate numerous weather patterns such as monsoon onset (Lau & Chan 1986), tropical cyclogenesis (Liebmann et al. 1994), and the frequency of precipitation (Bond & Vecchi 2003). On a larger scale, the MJO also interacts with modes of climate variability, such as the Arctic Oscillation (L'Heureux and Higgins 2008), the North Atlantic Oscillation (Cassou 2008), and the El Niño-Southern Oscillation (Hendon et al. 2007).

1.3 The MJO-QBO Relationship

Many recent studies suggest that MJO activity is greatly affected by the QBO throughout boreal winter. Marahall et al. (2017) and Son et al. (2017) found that approximately 40% of interannual variation in MJO amplitude during boreal winter was explained by the QBO. These studies also suggest that during the easterly phase of the QBO, MJO amplitude is more predictable and its teleconnections more distinct. Other research suggests that EQBO produces conditions more favorable to the development of deep convection for the MJO (Nishimoto & Yoden 2017). Additionally, the MJO has been found to be initiated more frequently and propagate more slowly during EQBO, which results in a longer duration of the MJO event. This also means that the MJO is more likely to propagate further into the western Pacific and over the Maritime Continent, which is a common barrier to MJO cycles (Zhang & Zhang 2018).

The QBO also has the potential to influence the MJO's teleconnections. One example is the North Pacific storm track (NPST). Wang et al. (2018) found that MJO-related changes to the NPST were larger in amplitude and spatially distinct during EQBO compared to WQBO. The study suggested these differences could be due to baroclinic energy conversion and a stronger MJO extratropical circulation, which in turn influences the NPST. Furthermore, the MJO and NAO are correlated at a lag of about 10 days after certain phases of the MJO. Recent studies have found that the MJO-NAO connection tends to be stronger during WQBO. Feng and Lin (2019) suggest that the QBO's modulation is likely due to anomalous subtropical westerly winds in the North Pacific during WQBO phases. This enhances the subtropical westerly jet, which is conducive to the propagation of extratropical Rossby waves associated with the MJO. Additional high-latitude westerly winds over the North Atlantic also support NAO development (Feng & Lin 2019).

Structural differences of the MJO during EQBO and WQBO are thought to be a primary driver behind the MJO-QBO relationship. During EQBO, positive temperature anomalies in the upper troposphere and cold cap anomalies near the tropopause tend to be stronger and more in phase with MJO convection anomalies. The temperature anomalies work together to reduce the static stability of the troposphere, and promote stronger MJO convection. (Hendon & Abhik 2018). This destabilization is additionally supported by cold anomalies at the tropopause throughout EQBO. The QBO's impact on static stability and the MJO could also be a consequence of the 11-year solar cycle. The largest amplitudes and occurrence rates of MJO events, as well as the weakest static stabilities have been found to occur during EQBO under solar minimum conditions. On the other hand, the smallest MJO amplitudes and strongest static stabilities were associated with solar maximum conditions during WQBO (Hood 2017).

Using a cloud-resolving model, Martin et al. (2019) tested the QBO's impact on the MJO by utilizing wind and temperature anomalies characteristic of the QBO. In experiments that only used temperature anomalies, it was found that MJO convection was amplified during EQBO compared to WQBO. The experiments that used only wind anomalies found much weaker results, which suggests QBO temperature anomalies are crucial to the QBO's influence on the MJO. This study also found that the relationship is dependent on the height and amplitude of the QBO temperature anomalies, where anomalies with lower altitude and higher amplitude have a

greater impact on MJO convection (Martin et al. 2019). Cloud-radiation feedback involving cirrus clouds may also play a role in this relationship. Cirrus clouds tend to form more frequently near the tropopause during EQBO, which result in a net-cooling effect in the lower stratosphere and warming in the troposphere. This works to further destabilize the upper troposphere, once again strengthening MJO convection (Son et al. 2017).

1.4 The El Niño-Southern Oscillation

As the world's leading pattern of interannual variability, the El Niño-Southern Oscillation (ENSO) plays a crucial role in affecting climate through ocean-atmosphere interactions. A primary feature of ENSO is its irregular oscillations in equatorial Pacific sea surface temperatures (SSTs), thermocline depth, tropical convection, and air pressure (Philander 1983). ENSO's timescale is considerably longer than that of the QBO and the MJO, with a period ranging anywhere from 2-7 years. As a coupled phenomena between the atmosphere and ocean, ENSO influences both, such as affecting the Hadley circulation through anomalous SSTs. (Bjerknes 1966). Changes in SST can influence circulation through zonal pressure gradients which in turn impact the strength of trade winds in the Pacific. This creates a positive feedback loop which once again leads to enhanced SST anomalies (Bjerknes 1969).

ENSO is additionally influenced by large-scale planetary waves. The delayed oscillator theory describes the propagation of Kelvin and Rossby waves due to forcing from wind stress. Westward-propagating Rossby waves are reflected back as Kelvin waves and lead to the delayed response that modulates the phases and timing of the ENSO cycle (Suarez and Schopf 1988). When these waves are excited, their propagation can also help distribute anomalous SSTs elsewhere, thereby affecting other regions of the globe. ENSO heating and cooling in the tropical Pacific can also provoke atmospheric wave trains which emanate from the tropics to the middle and high latitudes (Yang et al. 2018). One such example of this is the Pacific/North American teleconnection (PNA) pattern, in which geopotential height anomalies spread and can modulate temperature in the Northern Hemisphere during ENSO phases (Yu et al. 2012). ENSO phases can additionally alter the strength of zonal mean flows and displace jet streams that influence weather patterns outside of the tropics (Lu et al. 2008).

Another primary feature of ENSO is its diversity among individual events. Capotondi et al. (2015), reviewed ENSO events and their tendency to vary spatially, temporally, and in amplitude from event to event. The authors remark that warm ENSO events (El Niños) tend to be more diverse than cold events (La Niñas). All types of El Niño events are typically preceded by westerly wind events in the western and central tropical Pacific. These westerly wind events are influenced by factors such as the equatorial zonal SST gradient and ocean heat content, noting that heat content in the tropical Pacific influences the type of ENSO event that will develop. Capotondi et al. (2015) also mentions that stronger El Niño events tend to exhibit peak SST anomalies that extend further east, and have a more significant role in the heat budget for thermocline motions. Forecast models are able to adequately distinguish between types of ENSO

events up to six months prior, but show a warm bias in the eastern Pacific for certain events (Capotondi et al. 2015).

1.5 The ENSO-QBO Relationship

Many recent studies have explored ENSO's potential to influence the stratosphere. ENSO's effects on the stratosphere can be quite difficult to separate from those of the QBO, as shown by Wallace & Chang (1982). By using data from the Northern Hemisphere polar vortex throughout 21 winter seasons, the authors were unable to find any significant difference between the effects of ENSO and the QBO on the stratosphere. Furthermore, van Loon & Labitzke (1987) found that when using weak ENSO years, ENSO and the QBO phases tended to coincide. Maruyama and Tsuneoka (1988) found evidence that El Niño events may relate to and enhance the rapid downward propagation of westerly winds during the QBO. The authors note the importance of Kelvin wave intensity in contributing to the westerly wind descent, but suggest that the rapidity of descent in the QBO events they analyzed could not be achieved by Kelvin waves alone.

Observation-based studies such as Baldwin and O'Sullivan (1995) suggest that ENSO's influence on the lower stratosphere is limited to wave components such as amplitude, whereas ENSO's influence on the zonal-mean structure of the polar vortex is restricted to the troposphere. A hypothetical mechanism was developed by Gray et al. (1992) in which the QBO can modulate the timing of ENSO events. The mechanism uses meridional redistribution of deep convection in the tropical Pacific that happens as a response to QBO wind shear processes. It was found that during EQBO, the QBO-induced changes in pressure and circulation are favorable conditions for warm ENSO events. On the other hand, the conditions needed for cold ENSO events are consistent with WQBO (Gray et al. 1992). This posed an interesting scenario in which the QBO could be a major component in determining ENSO variability.

A major challenge in examining the ENSO-QBO relationship is the limited amount of sampling in the observational record. The relationship has also been found to be dependent on the sampling period, as discussed by Geller et al. (2016). This study found that QBO amplitudes tended to be larger during La Niña events compared to El Niño events, but only after around 1990. A possible reason for this relationship could be that deep convection during La Niña leads to a broader gravity wave phase speed spectrum, which in turn leads to larger QBO amplitudes. The measured deep convection during La Niña was likely at its strongest after 1990, whereas before this time period, El Niño events had a broader extent of deep convection (Geller et al. 2016).

1.6 Current Challenges

Modern general circulation models (GCMs) have great difficulty in capturing the QBO and its complex relationships with other phenomena. Kim et al. (2020) examined the QBO-MJO relationship in 30 models from the Coupled Model Intercomparison Project 6 (CMIP6). The authors found that some of the models were able to adequately simulate the QBO, but when

looking at MJO activity during each QBO phase, none of the models were able to find a significant difference beyond what was expected. This failure could potentially be due to the models' weaker amplitude of the QBO than what has been observed, especially near the tropopause (Kim et al. 2020). A similar result was found when examining the QBO-MJO link in the Global Ocean Mixed Layer configuration of the Met Office Unified Model (MetUM-GOML1). MetUM-GOML1 found an insignificant correlation between MJO amplitude and QBO winds in boreal winter, which contradicts the significant anti-correlation found in reanalysis. Reanalysis suggests that EQBO is connected to strong MJO activity over the Maritime Continent, while MetUM-GOML1 shows stronger MJO activity over the western Pacific. This bias could potentially be due to errors in the vertical structure of the MJO, or weak QBO-induced temperature anomalies (Lee and Klingaman 2018).

Another case involves subseasonal-to-seasonal (S2S) prediction models and the MJO-QBO connection. Lim et al. (2019) found that models did a better job predicting the MJO during EQBO winters compared to WQBO winters. When using the bivariate anomaly coefficient of 0.5, the MJO prediction skill was enhanced by up to 10 days. The authors also found that this enhancement was not sensitive to the initial amplitude of the MJO, which suggests that an improved MJO prediction skill was not solely due to a stronger MJO to begin with (Lim et al. 2019). However, another analysis of S2S models and MJO prediction skill showed different results. MJO prediction skill was still found to be higher for EQBO, but the correlation between QBO phase and MJO prediction skill was not statistically significant for most of the models examined. Thus the QBO in these models may not be directly affecting the MJO prediction skill (Kim et al. 2019). Bushell et al. (2022) examined cases from the Stratosphere-troposphere Processes And their Role in Climate (SPARC) Quasi-Biennial Oscillation initiative (QBOi), in which the QBO was better simulated from improvements in gravity wave tuning. However, the simulations used prescribed SSTs based on observations, which does not necessarily rectify the issue of limited sampling.

This thesis aims to explore the relationship between the QBO, the MJO, and ENSO using linear inverse modeling, with the goals of addressing these difficult challenges. Linear inverse modeling allows for an empirical, statistical-based analysis of these phenomena given the problems posed by limited sampling and poor performance in GCMs. In this thesis, linear inverse modeling will be used to expand sampling through forward integration in order to test how the nature of these relationships change with additional data. Dynamical filtering of the linear inverse model will also be utilized to separate dynamical climate processes and observe any nuances within the data. This methodology will assist in understanding the individual variability of these phenomena and how that affects their connections to each other.

Chapter 2

Data and Methods

2.1 Linear Inverse Modeling

Linear inverse modeling (LIM) is a technique used to analyze the dynamics of climate systems based on their observed statistics. The techniques and equations used in this study follow that of Penland and Sardeshmukh (1995), Henderson et al. (2020), and references therein. A system's evolution in time is given by the linear stochastic equation:

$$d\mathbf{x}/dt = \mathbf{L}x + \zeta \tag{1}$$

where $\mathbf{x}$ is the course-grained state vector, $\mathbf{L}$ is a matrix that represents the linearized dynamics of $\mathbf{x}$ as well as a linear approximation to the nonlinear dynamics, and ζ is the white noise forcing. The solution to the homogeneous term in (1) gives the deterministic evolution from an initial time t=0 to time t=τ:

$$\mathbf{x}(\tau) = \mathbf{G}_\tau \mathbf{x}(0) = exp(\mathbf{L}\tau)\mathbf{x}(0). \tag{2}$$

The term $\mathbf{G}_\tau$ is a propagator that evolves to $\mathbf{x}(\tau)$ from an initial condition $\mathbf{x}(0)$. Both $\mathbf{L}$ and $\mathbf{G}_\tau$ can be obtained using the covariance matrix of $\mathbf{x}$ at time t=0 ($\mathbf{C}_0$) and at lag τ ($\mathbf{C}_\tau$):

$$\mathbf{G}_\tau = \mathbf{C}_\tau \mathbf{C}_0^{-1}, \tag{3}$$

so that

$$\mathbf{L} = ln(\mathbf{G}_\tau)/\tau_0. \tag{4}$$

The white noise forcing can be further analyzed using the fluctuation-dissipation relation (Penland and Matrosova 1994). This is given as:

$$\mathbf{L}\mathbf{C}_0 + \mathbf{C}_0\mathbf{L}^T + \mathbf{Q} = 0 \tag{5}$$

where $\mathbf{Q}$ is the covariance matrix of the white noise forcing.

2.2 Data

Data for the LIM is supplied by the Japanese 55-year Reanalysis (JRA-55; Kobayashi et al. 2015). The four variables used in this study are sea surface temperature (SST), column-integrated heating (Q_1), 30- and 50-mb zonal wind (U_{30_50}), and the 750-hPa streamfunction (Ψ). The

spatial resolution is regridded from its original 1.25º x 1.25º resolution to give a new resolution of 2º x 2º. This is done in order to better capture the dynamical features being analyzed by reducing small-scale variability. The data spans from 1958 through 2018, and is recorded on 6-hour intervals, which are then averaged to get daily values. The climatological mean values are subtracted from each variable dataset and the seasonal cycle is removed to obtain anomalies. A 5-day running mean is applied, and each of the 4 variable datasets is sliced between 25ºN and 25ºS to isolate the tropical latitudes. The empirical orthogonal functions (EOFs) and principal components (PCs) for each variable are computed with only a specified amount of variance kept for each field. The PCs are subsequently loaded into the state vector **x** so that

$$\mathbf{x}(t) = \begin{bmatrix} SST \\ Q_1 \\ U_{30\_50} \\ \Psi \end{bmatrix}. \tag{6}$$

The finalized state vector is expressed in reduced EOF space with a retained variance of 53%, 34%, 93%, and 56% for SST, Q_1, U_{30_50}, and Ψ respectively. The variances are explained by the leading 8, 30, 4, and 7 EOFs for each respective field, for a total of 49 principal components. The amount of variance kept is chosen based on values from similar studies (Henderson et al. 2020, Winkler et al. 2001), as well as the numerical stability of the model.

2.3 Testing the LIM

In this study, the matrix **L** is derived using a specified lag of τ_0=5 days in (4). The lag is selected based on the τ-test from Penland and Sardeshmukh (1995), and the timescale of variability that is being examined. Figure 2 shows the result of the τ-test for τ_0 values of 1 through 20 days. The curves represent the Euclidian norms of the submatrices $\mathbf{L_n}$ of **L** for each τ_0. As discussed in Penland and Sardeshmukh (1995), **L** should be independent of the chosen τ_0. A greater risk of error arrises when the chosen lag is larger than half of the period of the smallest oscillation in the system being analyzed. As is observable in the figure, there's a prominent peak around τ_0=15 days, which may correspond to roughly half of the shortest period of an MJO event. The chosen τ_0 should be shorter than this peak. We chose 5 days since an MJO phase is roughly this long, as done in Henderson et al. (2020).

An additional test of the validity of the LIM is to plot the forecasts of error variance as a function of the lead time (Penland 1989, Winkler et al. 2001). This is done to test whether the error is growing as predicted by theory. The forecast error variance, $\delta(\tau)$, is equal to $\langle \sigma(\tau)^T \sigma(\tau) \rangle$, which is the trace of the error covariance matrix. This can be derived from (2) at a time $t + \tau$ to yield:

$$\langle \sigma(\tau)\sigma(\tau)^T \rangle = \mathbf{C}_0 - \mathbf{G}_\tau \mathbf{C}_0 \mathbf{G}_\tau^T. \tag{7}$$
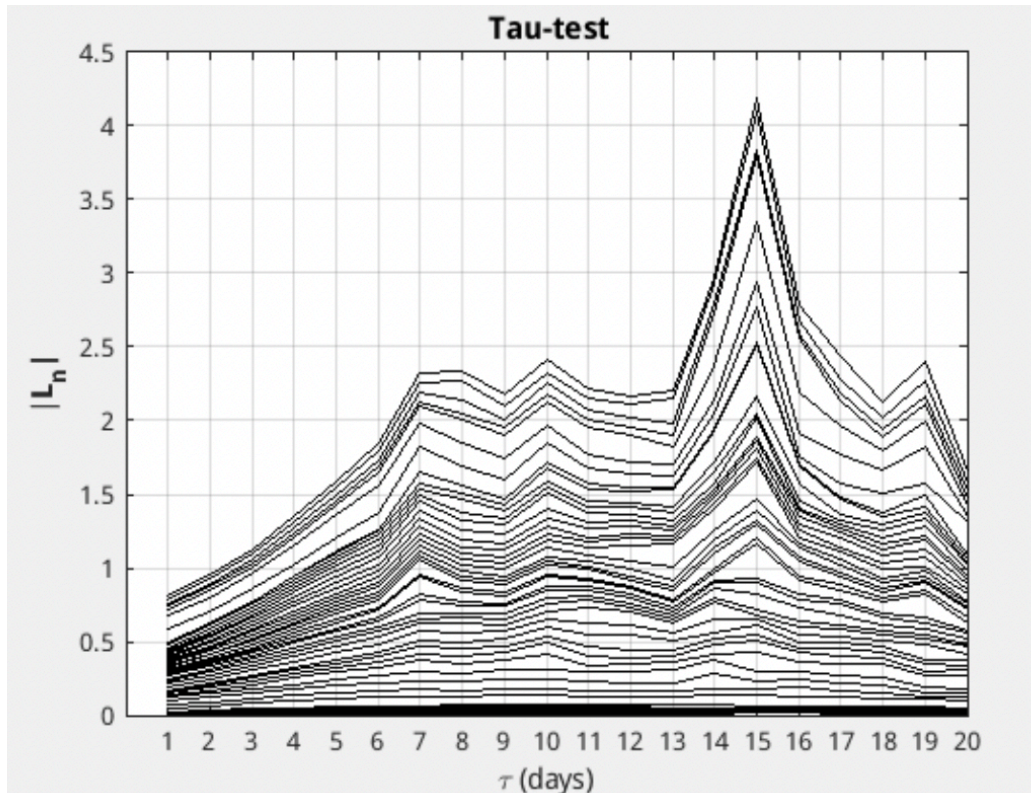
FIGURE 2: The τ-test as in Penland and Sardeshmukh (1995). The curves represent Euclidian norms of **L** and its submatrices **L$_n$** for varying lag times in days.

The forecasted error variance plot is shown in Figure 3 as a function of lag (τ), with circles representing the actual error from the LIM, squares representing persistence forecasts, the dashed line representing the theoretical error, and the autoregressive (AR1) forecast plotted as triangles. The actual error curve follows the theoretical error curve rather closely, which is a good indicator that the error is growing as predicted. Still, for the first 10 days, the actual error curve is a bit steeper than the theoretical curve, meaning that the LIM's error is growing at a slightly faster rate than theory. Winkler et al. (2001) notes a similar discrepancy between the actual and theoretical error curves, stating that this could be due to a weak correlation between the initial state and forecast error for short lead times. Any differences could also be attributed to a small amount of nonlinearity in the model. Penland and Sardeshmukh (1995), who used a similar process but with SST anomalies, run into a similar issue. The authors describe the difficulty of the system to make accurate ENSO predictions during the warm phases, and how this could be a possible explanation to the larger error at short lead times in their monthly LIM. Importantly, actual error is much smaller than the persistence and AR1 forecasts, indicating that the LIM has greater forecast skill.
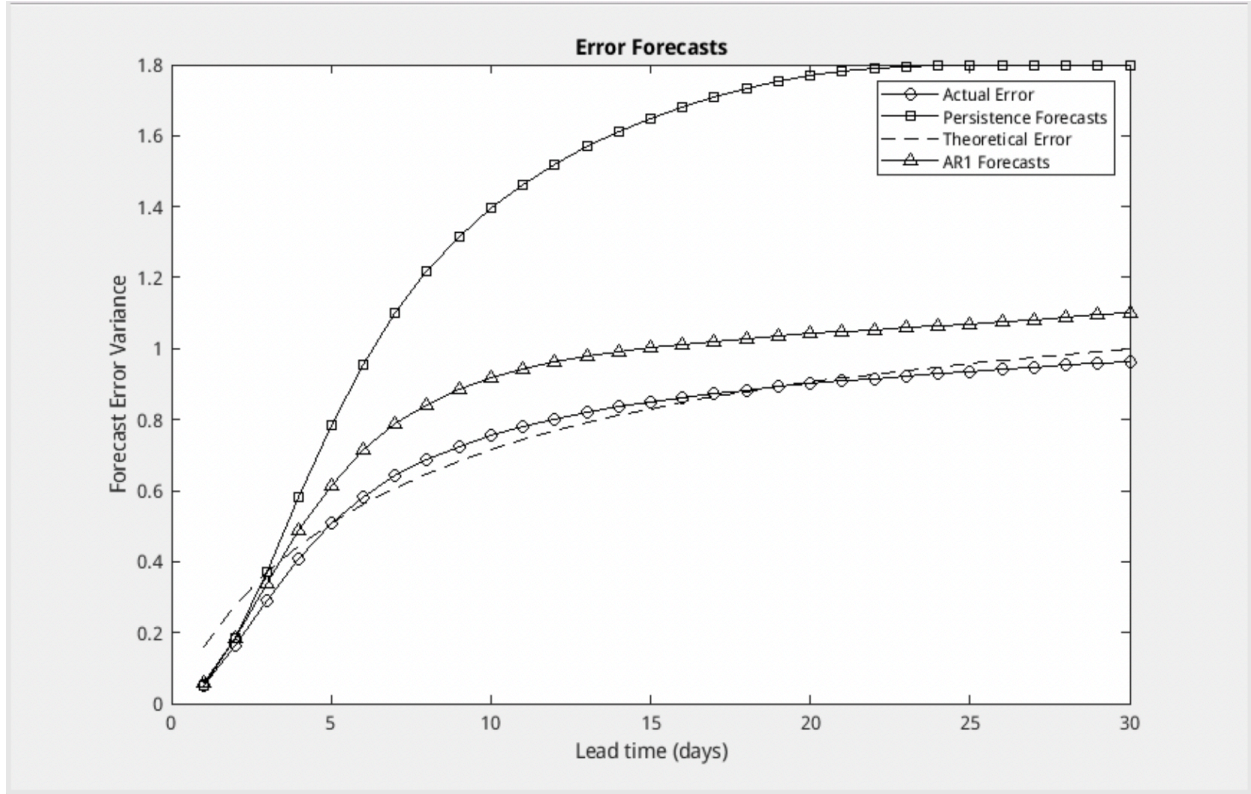
FIGURE 3: Error variance of forecasts for the LIM data as a function of lead time (circles). Theoretical error variance as predicted by (7) (dashes). Error variance of persistence forecasts (squares). Error variance of AR1 forecasts (triangles).

The growth and decay of a system over a time interval τ can be written as:

$$\mu(\tau) = \frac{\mathbf{x}(0) \cdot \mathbf{G}^T \mathbf{G}_\tau \mathbf{x}(0)}{\mathbf{x}(0) \cdot \mathbf{x}(0)} \tag{8}$$

(Penland and Sardeshmukh 1995). This growth can be plotted as a function of τ to obtain the maximum amplification (MA) curve. Figure 4 shows the maximum amplification curves for the first three EOFs of the combined data. The first two EOFs have an initial peak at a lag of about 6 days. The first EOF also has an additional peak at around 260 days. The peak at longer timescales is likely due to the incorporation of the stratosphere into the LIM, and a consequence of the QBO. The peaks at 6 days could possibly be representative of the MJO influence, but more research is needed to confirm this.

2.4 Dynamical Filtering

Filtering the eigenvectors and corresponding eigenvalues of $\mathbf{L}$ serves as a way to isolate the individual dynamical processes happening within the data. Following the methodology of
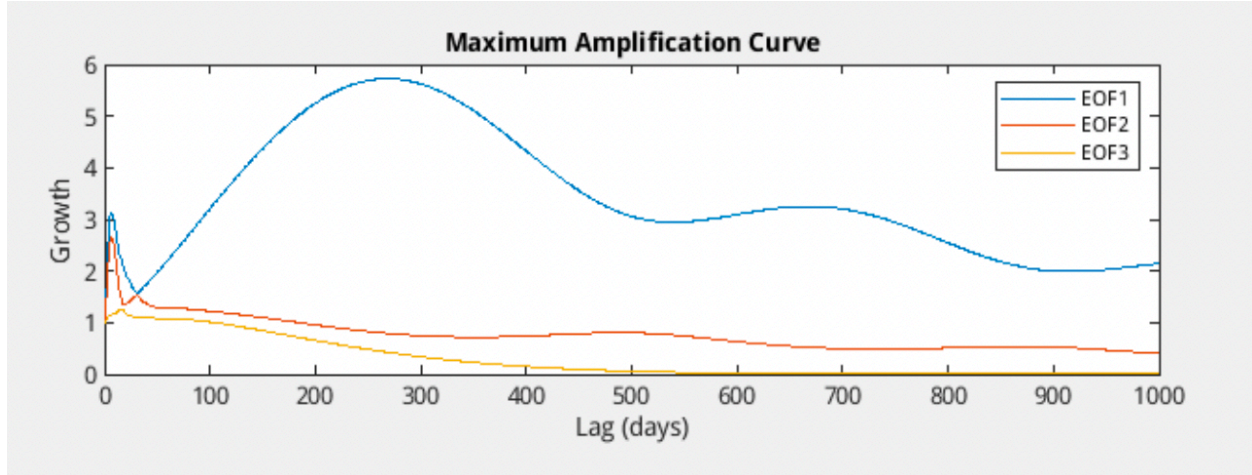
FIGURE 4: Maximum amplification (MA) curves for the first 3 EOFs of the combined data as a function of lag times. EOF 1 (blue). EOF 2 (red). EOF 3 (yellow).

Penland and Matrosova (2006) and Newman et al. (2009), the state vector $\mathbf{x}$ can be decomposed into subspaces using the following equation:

$$\mathbf{x}(t) = \Sigma_j \mathbf{u}_j \alpha_j(t) \tag{9}$$

where $\alpha_j(t)$ is the projection coefficient, $\mathbf{u}$ represents the eigenvectors of $\mathbf{L}$, and j denotes the 49 eigenmodes of $\mathbf{L}$ that are being summed over. One important aspect to note is that the modes of $\mathbf{L}$ are non-orthogonal. This property of the dynamical operator can lead to interference among the filtered subspaces which make up the full data. Filters were defined to isolate four subspaces: stratosphere-troposphere-SST modes, tropospheric internal modes, stratospheric internal modes, and troposphere-SST modes. Physically, the stratosphere-troposphere-SST modes represent covariability across the stratosphere, troposphere and ocean surface. Similarly, the troposphere-SST modes indicate covariability across the troposphere and ocean surface, but are independent of the stratosphere. Grouping for each filter is based on the amplitude of each eigenmode for each variable, defined by the inner dot product. This coincides with the frequency and e-folding time of the eigenvalues, as well as the relative variance contributions for each state vector variable. Figure 5 shows these relative contributions, where the fractional variance of each variable is plotted for each of the 49 eigenmodes. For example, modes 44 and 45 only have variance in the 30- and 50- mb zonal wind, so these modes are representative of processes internal to the stratosphere. The companion plot to this is Figure 6, in which the e-folding time is plotted against the frequency for the eigenmodes. The filter names, as well as the corresponding eigenmodes are displayed in Table 1. The state vector is filtered by summing (9) only over the modes that correspond to a subspace, resulting in a filtered state vector for each subspace.
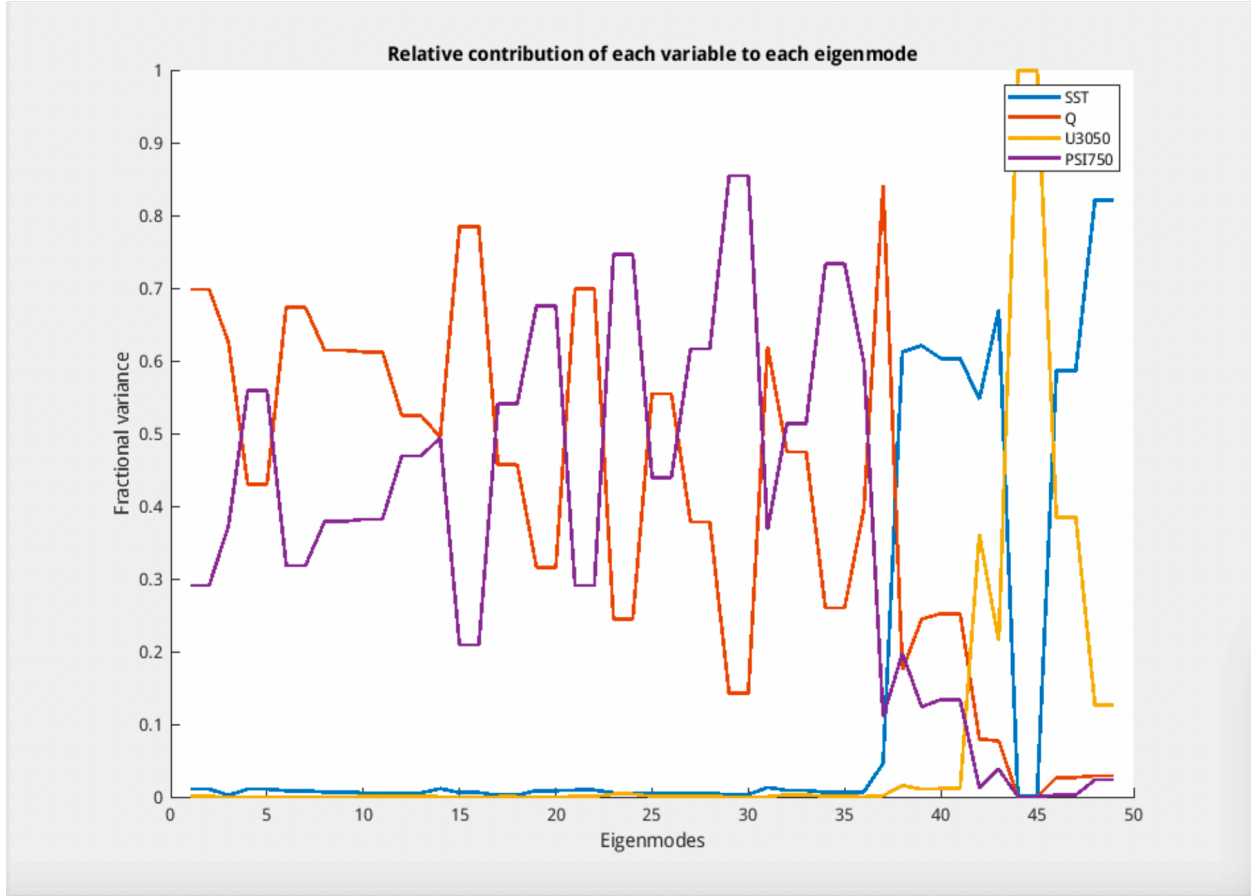
2.5 Forward Integration

FIGURE 5: Fractional variance of SST (blue), Q_1 (red), U_{30_50} (yellow), and Ψ (purple) for each eigenmode.

As discussed in the introduction, a big obstacle to QBO research is the scarcity of data. As seen in Penland and Matrosova (1994), (1) can be integrated forward to supply additional data points to the original time period, forming climate simulations. This procedure incorporates **L** and the covariance matrix of the white noise forcing **Q** from the fluctuation-dissipation relationship mentioned above. After integration, the climate run state vector time series **X** is given as:

$$\mathbf{X}(t + \frac{\Delta}{2}) = \frac{Y(t) + Y(t + \Delta)}{2} \tag{10}$$

where

$$Y(t + \Delta) = Y(t) + \sum_j \mathbf{L}_j Y(t)\Delta + \sum_i \mathbf{q}_i \sqrt{\eta_i \Delta \mathcal{R}_i}. \tag{11}$$

The summation indices j and i refer to the 49 EOFs kept, where j corresponds to those from the original state vector **x**, and i for the EOFs of **Q**. A 365,000-day time series is created, where Δ

=1/24 days, or a time step of 1 hour. The variable $\mathcal{R}$ represents a set of randomly-generated numbers for each time step that are normally distributed and have unit variance. **L** is the dynamical system matrix, and **q** and η are the eigenvectors and eigenvalues of **Q** respectively.

The same filtering methodology discussed in section 2.4 is used for the climate run time series **X** to isolate the same subspaces, but now with more data points.
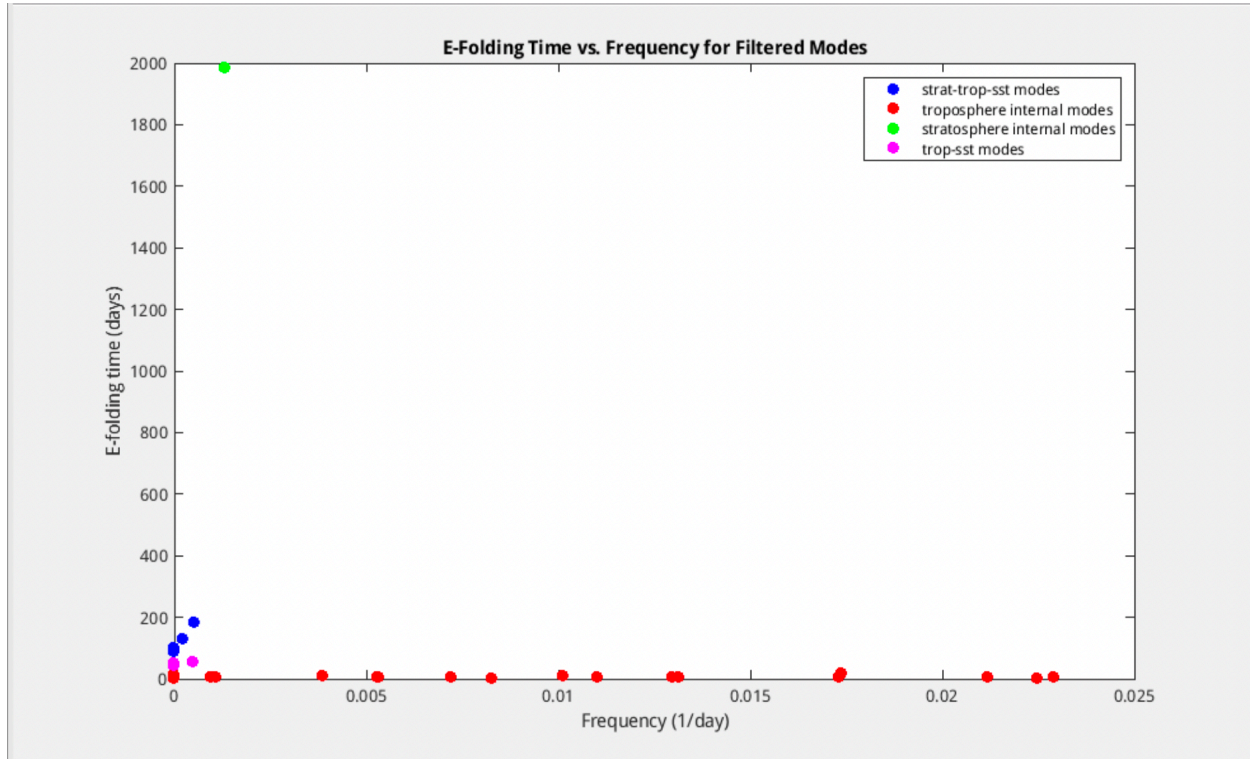

FIGURE 6: E-folding time vs. frequency for filtered eigenmodes. Filter names are strat-trop-sst modes (blue), troposphere internal modes (red), stratosphere internal modes (green), and trop-sst modes (pink).

Filter Name	Eigenmodes	Range of Frequencies (1/day)	Range of E-Folding Times (days)
Stratosphere-Troposphere-SST Modes	42,43,46-49	0-0.0005	89-184
Tropospheric Internal Modes	15-37	0-0.023	3.7-17
Stratospheric Internal Modes	44,45	0.0013	1,987
Troposphere-SST Modes	38-41	0-0.00048	42-55

TABLE 1: Filter names and the corresponding eigenmodes, range of frequencies, and range of e-folding times for each filter.

Chapter 3

Results & Discussion

3.1 Hovmöller Diagrams

With the newly defined subspaces, each filtered variable in the state vector can be analyzed using time vs. longitude plots, otherwise known as Hovmöller diagrams. With these plots, one can observe how each property of the dynamical system is progressing through space and time. The filters give insight into where the most variability resides for each field, or rather which subspace is having the biggest impact on the full, unfiltered data. The subspaces additionally show the component of the unfiltered data that can be attributed to covariability across the ocean surface, troposphere, and stratosphere, as apposed to internal variability. Since there tends to be a lot of overlap in ENSO and MJO signals, this poses an interesting obstacle for studying these patterns. To remedy this, we look at seasons where both ENSO and the MJO have strong activity, as well as examine years that were considered to be ENSO neutral (neither an El Niño nor La Niña event), but still had strong MJO activity. These specific conditions are determined using the extended Multivariate ENSO Index (MEI.ext; NOAA), and phase space diagrams of MJO activity (Australian Government Bureau of Meteorology).
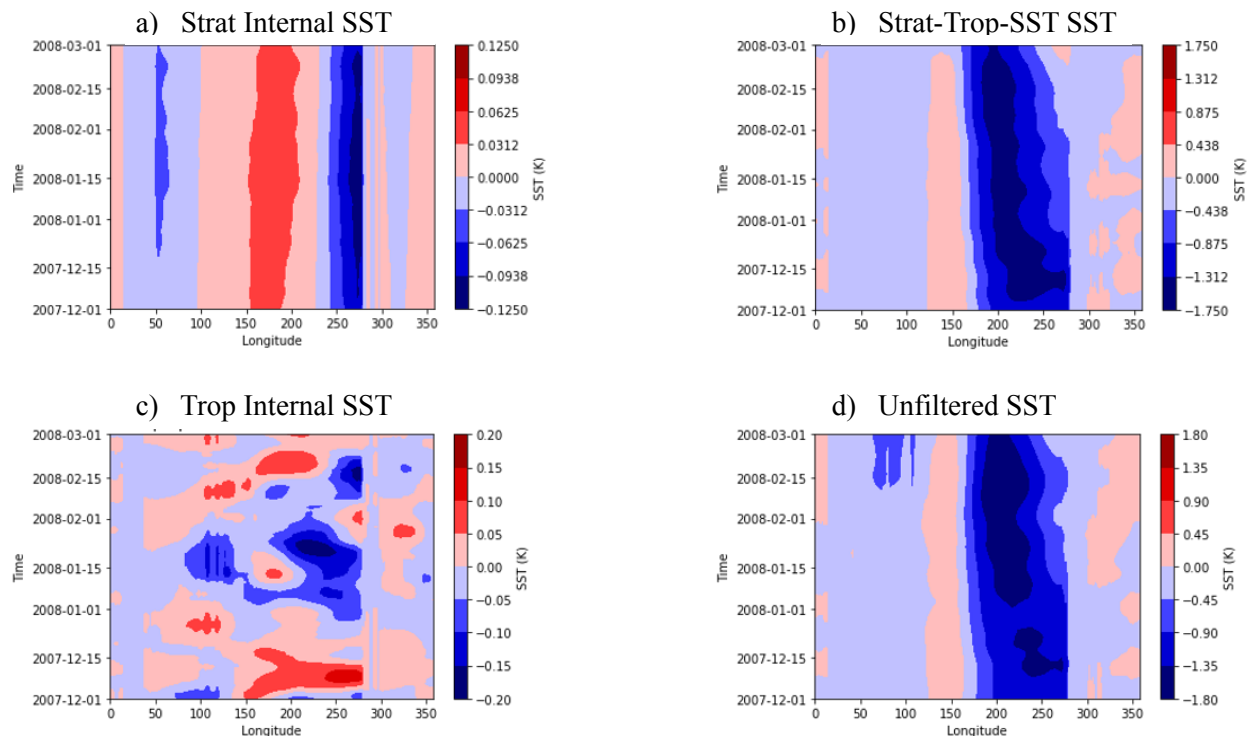

FIGURE 7: Time vs. longitude plots of SST values during boreal winter of 2007-2008. SST is plotted for the stratospheric internal subspace (a), the strat-trop-sst subspace (b), the tropospheric internal subpace (c), and the full data (d).

We first focus on winter 2007-2008, when both a strong La Niña event and a strong MJO event occurred. The data is averaged from 10ºS to 10ºN in order to better capture the features. The time dimension is also restricted to only portray data during boreal winter (December-February), which is an ideal time period to observe active ENSO and MJO events. Figure 7 shows SST values during this time period for the stratospheric internal subspace, the tropospheric internal subspace, the stratosphere-troposphere-SST subspace, and the full unfiltered space. In both the full and strat-trop-SST space, a persistent signal of cold SST anomalies is observable that is indicative of a La Niña event. In the tropospheric internal space, the MJO's impact is evident. Patches of warm and cold SST anomalies are present in this subspace, which alternate in time. The eastward propagation of the MJO also appears in this panel, as shown by the slight upward tilt in the pattern. The signal stops rather abruptly near 300ºE (60ºW), likely due to cold SSTs in the eastern Pacific which inhibit further eastward propagation of MJO convection. All the filtered panels combined will add up to the unfiltered data (note trop-SST filtered data is not shown; Fig. 6, pink circles), which closely resembles the strat-trop-SST panel due to the significant influence of ENSO on the unfiltered data. The unfiltered data is slightly greater in magnitude (note difference in label bar), but the shape is fairly close to the strat-trop-SST pattern. The MJO-like pattern that is observable in the internal troposphere space is largely hidden in the unfiltered data.
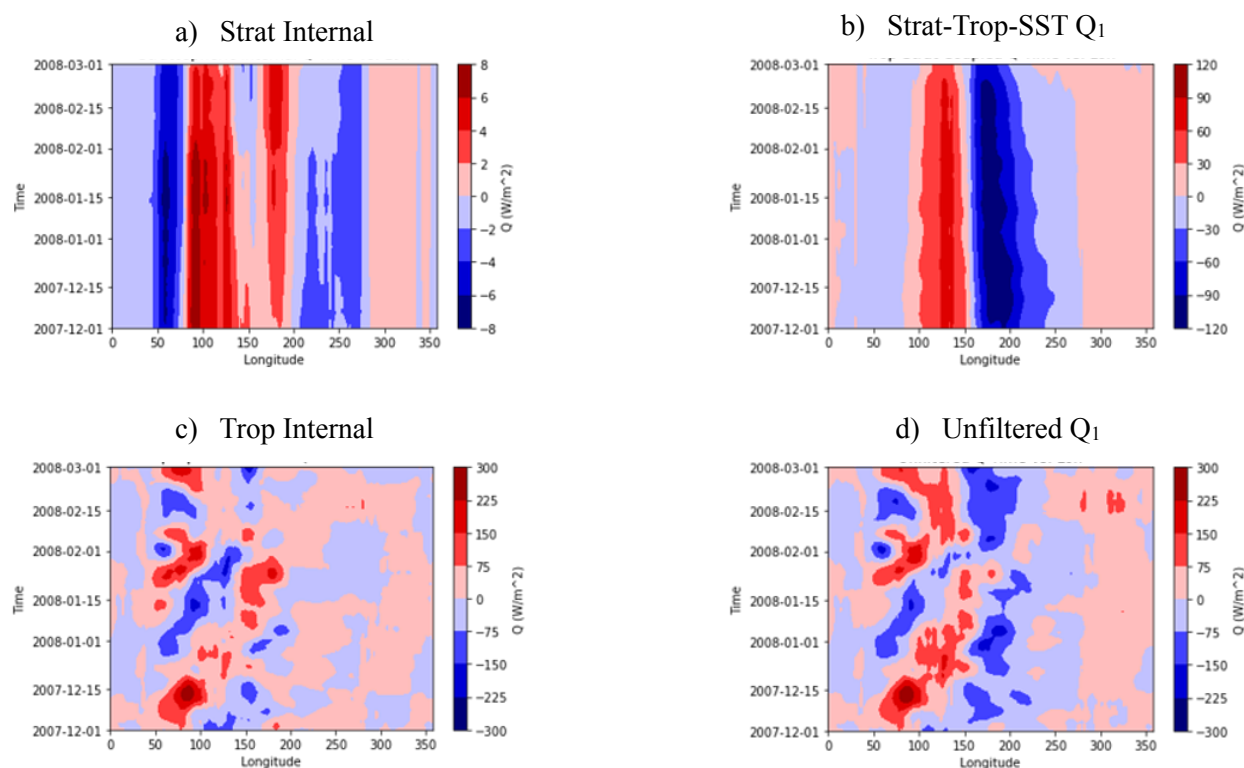

FIGURE 8: Time vs. longitude plots of Q_1 values during boreal winter of 2007-2008. Q_1 is plotted for the stratospheric internal subspace (a), the strat-trop-sst subspace (b), the tropospheric internal subpace (c), and the full data (d).

Figure 8 shows the same winter season, but this time with column integrated heating. As previously mentioned, the sloped anomalies in the internal troposphere panel indicate the eastward propagation of the MJO. In the strat-trop-SST space, heating anomalies that are consistent with La Niña are present. Cold anomalies persist through time in the central and eastern Pacific, while the warm anomalies are restricted to the western Pacific. Overall, the internal troposphere space is having the biggest impact on the full heating data, as noted by the similar magnitude of anomalies as well as a similar pattern of alternating positive and negative anomalies. The heating anomalies associated with La Niña are also evident near the Central Pacific, with some constructive and destructive interference between the strat-trop-SST and trop internal subspaces.
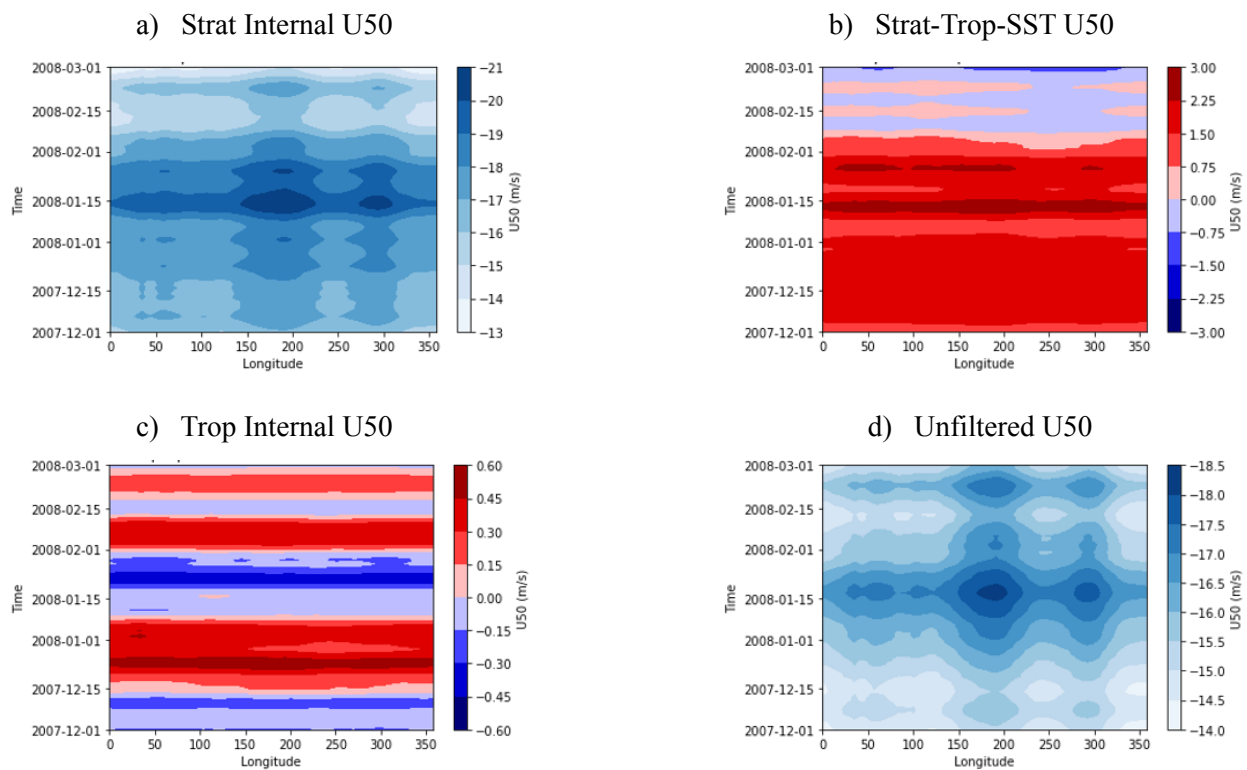

FIGURE 9: Time vs. longitude plots of U50 values during boreal winter of 2007-2008. U50 is plotted for the stratospheric internal subspace (a), the strat-trop-sst subspace (b), the tropospheric internal subpace (c), and the full data (d).

The final set of figures for this winter season show the 50-mb zonal wind in each subspace (Figure 9). In the internal stratosphere panel, the negative anomalies that persist over time indicate an easterly phase of the QBO. This panel also has the largest contribution to the unfiltered space, and is even slightly bigger in magnitude than the unfiltered data. This is likely due to destructive interference from the second and third panels that is weakening the overall signal. Note the strat-trop-SST subspace contains westerly anomalies, suggesting the La Niña event is associated with westerly anomalies in the stratosphere. Differences in the persistence of

the patterns for each variable indicate the timescales of the phenomena being analyzed. ENSO and the QBO show longer signals that can stretch across multiple seasons and years, while the MJO signal is shorter, due to its intraseasonal nature.

a) Strat Internal SST

b) Strat-Trop-SST SST

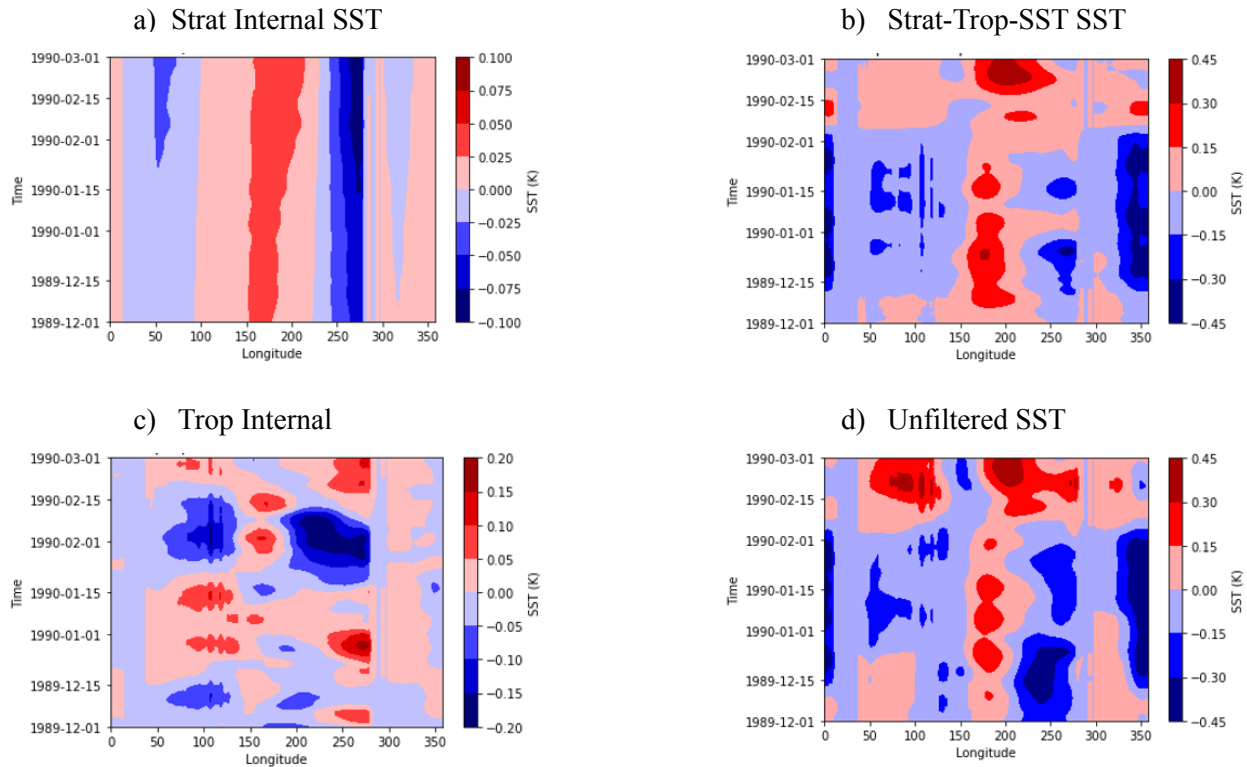c) Trop Internal

d) Unfiltered SST

FIGURE 10: Time vs. longitude plots of SST values during boreal winter of 1989-1990. SST is plotted for the stratospheric internal subspace (a), the strat-trop-sst subspace (b), the tropospheric internal subpace (c), and the full data (d).

An additional case examined here is the 1989-1990 boreal winter season, in which there was strong MJO activity happening during an ENSO neutral season. Figure 10 contains the SST plots. Once again, in the internal troposphere space, the MJO's impact on sea surface temperature can be observed in the patchy and alternating pattern. However, in the strat-trop-SST space, a different pattern is present than what could be seen during an active ENSO year. Without the presence of ENSO, the persistent and strong SST signal is absent, and a less coherent pattern remains. When added together to produce the fourth panel, the strat-trop-SST space is notably having a large effect on the overall shape and magnitude of the anomalies, with clear interference from the internal troposphere subspace.

For the case of heating in Figure 11, once again the MJO's signal is prominent in the internal troposphere panel. A slight amount of interference from the strat-trop-sst space changes the overall shape and magnitude of the full space. This may be a consequence of the weak SST anomalies (Figure 10) or stratospheric influence. Figure 12 shows the stratospheric zonal wind. It is once again an easterly phase of the QBO, as indicated by the persistent negative zonal wind

anomalies in the stratospheric internal subspace. Interestingly, the strat-trop-SST anomalies act to amplify the easterly anomalies in late winter. It is not clear what the strat-trop-SST zonal wind anomalies are from Figure 12. This may due to the averaging across latitudes done for these figures, given that Section 3.3 finds that the anomalies within this subspace are asymmetric about the equator.
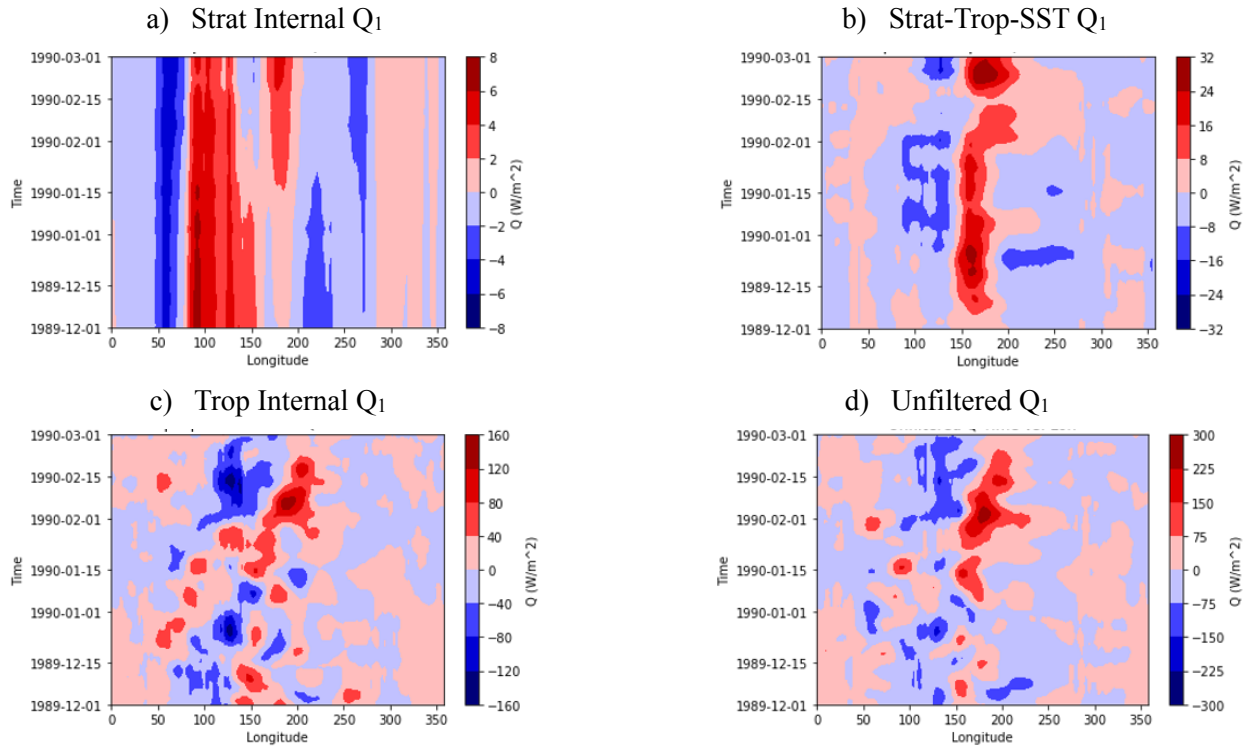

FIGURE 11: Time vs. longitude plots of Q_1 values during boreal winter of 1989-1990. Q_1 is plotted for the stratospheric internal subspace (a), the strat-trop-sst subspace (b), the tropospheric internal subpace (c), and the full data (d).
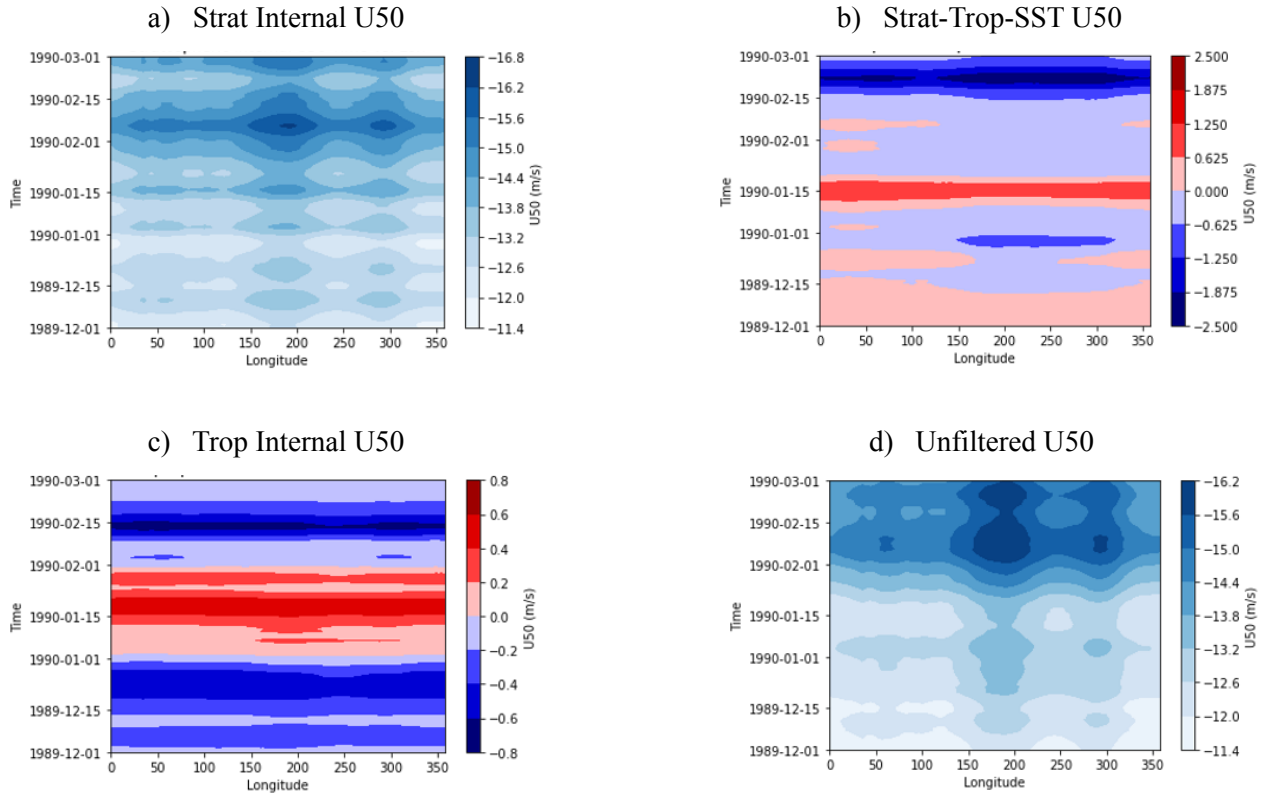
FIGURE 12: Time vs. longitude plots of U50 values during boreal winter of 1989-1990. U50 is plotted for the stratospheric internal subspace (a), the strat-trop-sst subspace (b), the tropospheric internal subpace (c), and the full data (d).

3.2 Power Spectra

Using the LIM climate run data, power spectra plots are created for the leading three PCs of each state vector variable (Figure 13). The spectra is calculated for the full unfiltered data (black line), as well as for the strat-trop-SST space (blue), the internal troposphere space (red), the internal stratosphere space (green), and the trop-SST space (pink). To calculate the power spectral density, a Hanning window with 1000-day segments is applied to each variable, with an overlap of 500 days. The first row of Figure 13 shows the SST power spectra. The first two EOFs of SST represent ENSO (Deser et al. 2010). This aligns well with the fact that the majority of the power for SST is captured within the strat-trop-SST subspace, in which ENSO resides. The curves are initially peaking at a frequency of about 500 days, which corresponds to longer, interseasonal timescales characteristic of ENSO. A small amount of power is also coming from the trop-SST subspace, and once again interference among the filtered spaces is likely lowering the overall power in the unfiltered data. Since the full space is not the sum of the variance from the other filters, this suggests that the subspaces are not orthogonal. The non-normality of the filters highlights the importance of a linear inverse model for this type of analysis. The second row shows plots for Q_1. For the first principal component, prominent peaks are observable in both the trop-strat-SST and internal troposphere subspaces. ENSO is once again captured in the strat-trop-
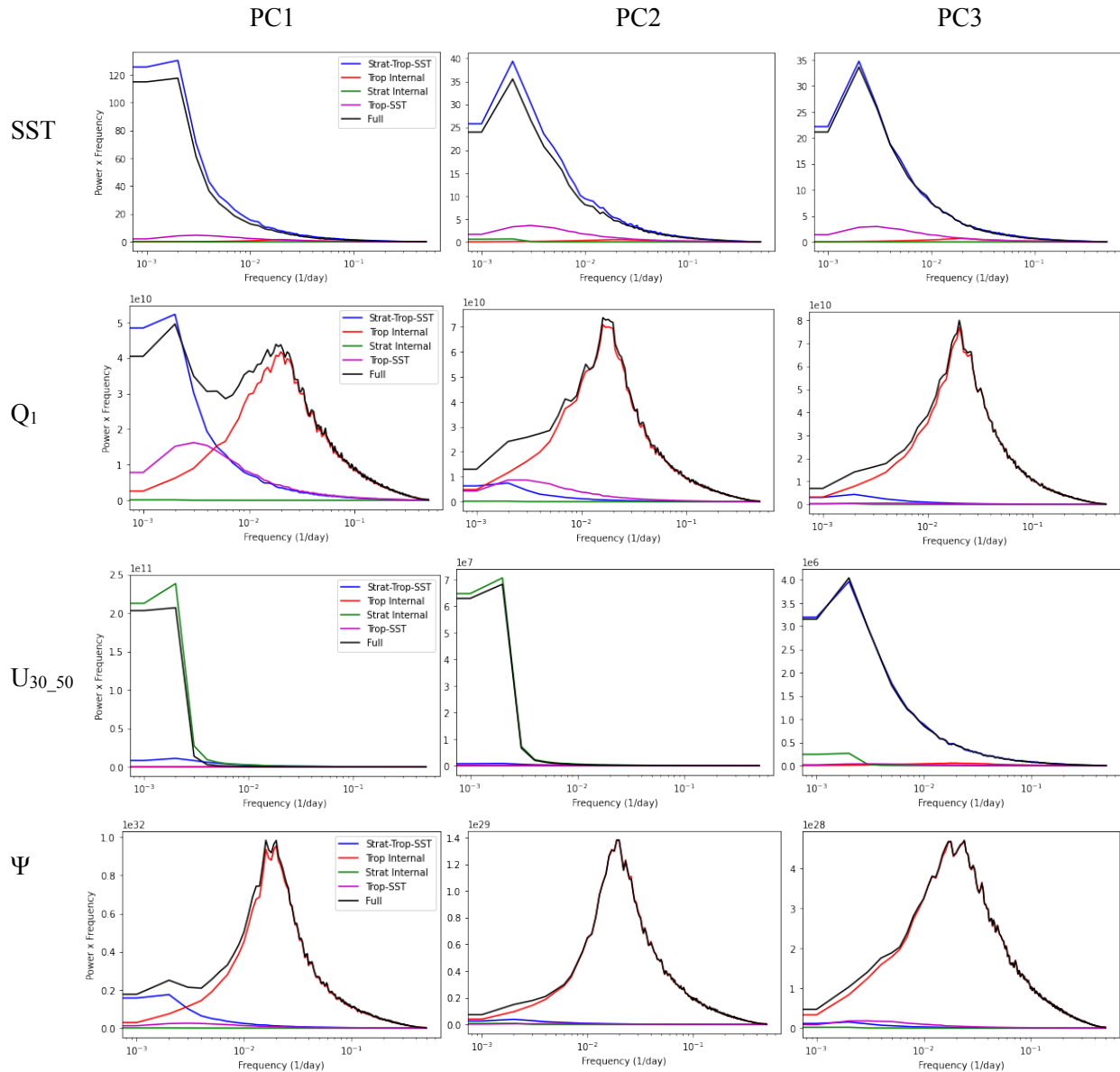
FIGURE 13: Power spectra for the first three PCs of SST (first row), Q_1 (second row), U30_50 (third row), and Ψ (bottom row). Spectra calculated using the full data are depicted by the black line. The spectra for each filtered subspace are additionally calculated: strat-trop-SST (blue), tropospheric internal (red), stratospheric internal (green), and trop-SST (pink).

SST space, whereas the internal troposphere space represents phenomena on intraseasonal timescales, such as the MJO.

The second and third principal components primarily peak in those intraseasonal timescales, at a frequency of approximately 50 days. The third row of plots corresponds to the power spectra for the 30- and 50-mb zonal wind. The first two principal components have peaks at low frequencies, which is representative of QBO timescales. The power of the first two PCs is largely

internal to the stratosphere (i.e. the QBO mode), as shown by this filter's large contribution to the overall power. The third principal component, however, shows a different story. Interestingly, the power is primarily captured by the strat-trop-SST subspace. A further exploration of this is shown in the paragraph that follows. Finally, the last row of figures shows the power spectra for Ψ. All three PCs show peaks in the intraseasonal timescales, best represented by the internal troposphere subspace. This makes sense given that the streamfunction is calculated at 750-hPa, within the troposphere.

To further explore the activity shown in the third PC of zonal wind, Figure 14 depicts the spatial pattern for the third EOF of U_{30_50}. Though the signs in the plot are arbitrary, it's observable that when the pattern is increasing or decreasing north of the equator, the opposite is happening below. There's also some asymmetry in the magnitude of the signals longitudinally. We cannot say for certain how much of this pattern aligns with significant ENSO activity. However, since the first two EOFs of zonal wind describe the QBO, this work suggests that the third EOF, which is orthogonal and therefore unrelated to the QBO EOFs, may be essential to understanding the stratospheric wind relationships with ENSO and the MJO. More research is needed to assess the significance of this pattern and interplay between the troposphere and stratosphere.
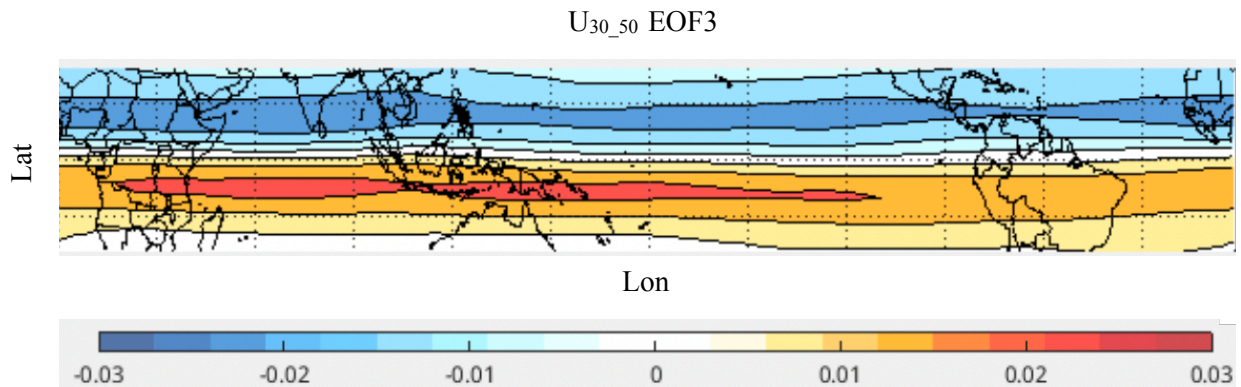

FIGURE 14: Spatial pattern for the third EOF of U_{30_50}.

3.3 Composites

Time-averaged composite maps are a useful tool for analyzing spatial patterns in the data. Using the strat-trop-SST subspace, the state vector variables can be compared based on how they look during different phases of the QBO and ENSO. QBO phases are determined using the 50-mb zonal wind data, where an easterly phase corresponds to zonal wind less than 0 m/s, and a westerly phase with zonal wind greater than 0 m/s. ENSO phases are determined using the first PC of the SST data, representing an eastern Pacific ENSO index similar to a Niño 3.4 index (L'Heureux et al. 2013). An El Niño phase occurs when SST values exceed 0.5 K, and a La Niña phase for SST values less than -0.5 K. ENSO neutral phases correspond to all points that fall between these bounds.
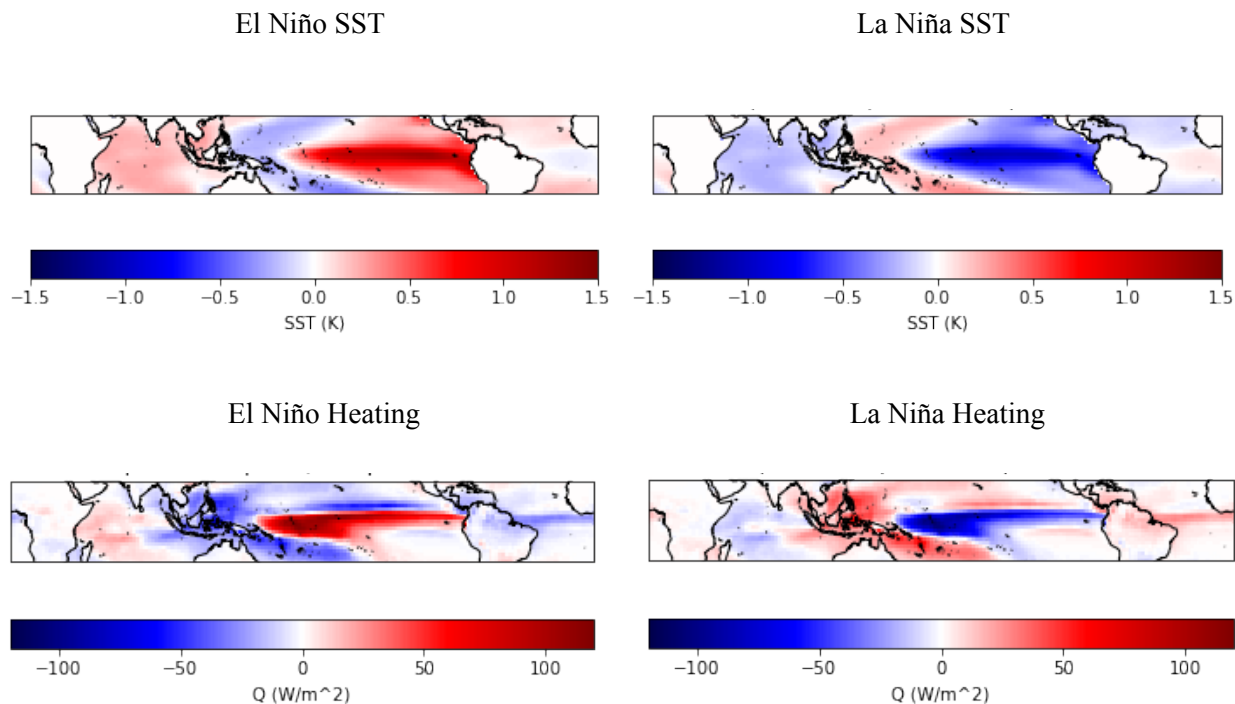
El Niño SST

La Niña SST

El Niño Heating

La Niña Heating

FIGURE 15: Time-averaged composite maps of SST
and Q_1 during El Niño events vs. La Niña events.

Figure 15 depicts time-averaged sea surface temperature and heating during both El Niño and La
Niña phases of ENSO. The plots look as expected, with warmer (colder) than average SSTs
during El Niño (La Niña) over the central and eastern Pacific Ocean. Based on the ENSO index
being used, it's important to note that these phases are representative of eastern Pacific ENSO
events.

In Figure 16, composites are created using only ENSO neutral data for SST and heating. The
data is additionally partitioned by QBO phase to give insight into how the QBO effects these
variables without the impact of ENSO. In both the heating and SST plots, the anomalies appear
stronger throughout the westerly phase of the QBO. The anomalies also have similar signs over
the Pacific Ocean, but differ over the Indian Ocean and Maritime Continent, where the
amplitudes are also weaker. It's difficult to say whether a specific QBO phase is directly
impacting the tropical troposphere, since QBO wind and temperature anomalies do not travel
significantly below the tropopause (Baldwin et al. 2001). These patterns are likely a consequence
of having limited sampling for data that is both ENSO neutral and EQBO/WQBO.

Figure 17 depicts 50-mb zonal wind composites using values from the strat-trop-SST dataset.
The data is further separated into both ENSO and QBO phase. Composites were also created
using the climate run data (Figure 18). In the El Niño and EQBO phase, both the original and
climate run plots show asymmetry in the signal around the equator that is not present in the
WQBO phase during El Niño. The band of positive anomalies around the equator in both the

EQBO neutral ENSO and La Niña phases becomes much narrower in the climate run composites. Compared to the observational record, the WQBO La Niña signal becomes more asymmetrical with more positive anomalies in the climate run plots. The additional data points supplied by the climate run give further insight into what spatial patterns are most prominent throughout the various phases.
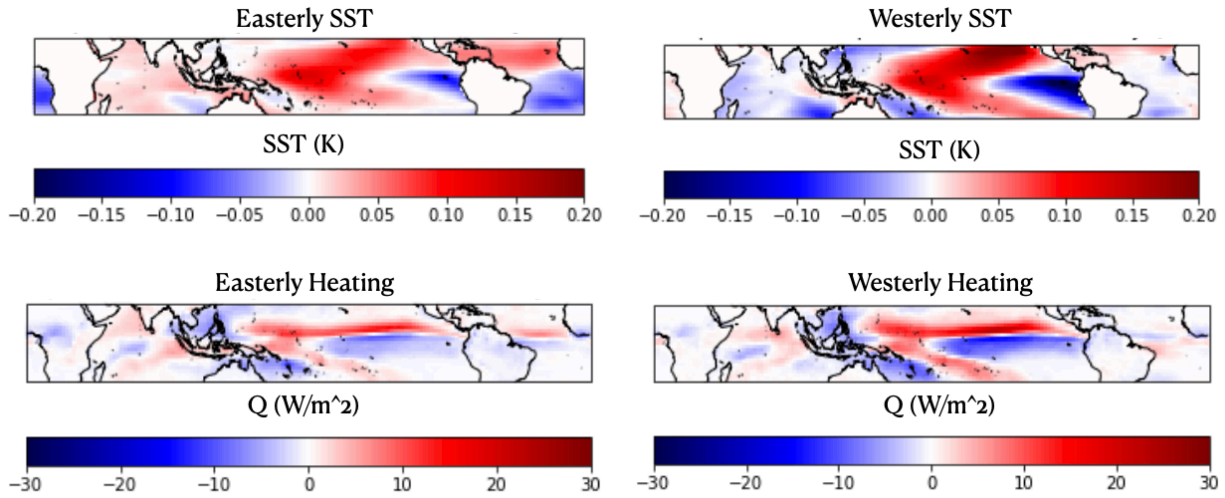
FIGURE 16: Time-averaged composite maps of SST and Q_1 during ENSO neutral events, additionally divided by QBO phase.

FIGURE 17: Existing record composite maps of 50-mb zonal wind during El Niño, La Niña, and ENSO neutral events, additionally divided by QBO phase.

EQBO   WQBO

El Niño

La Niña

Neutral
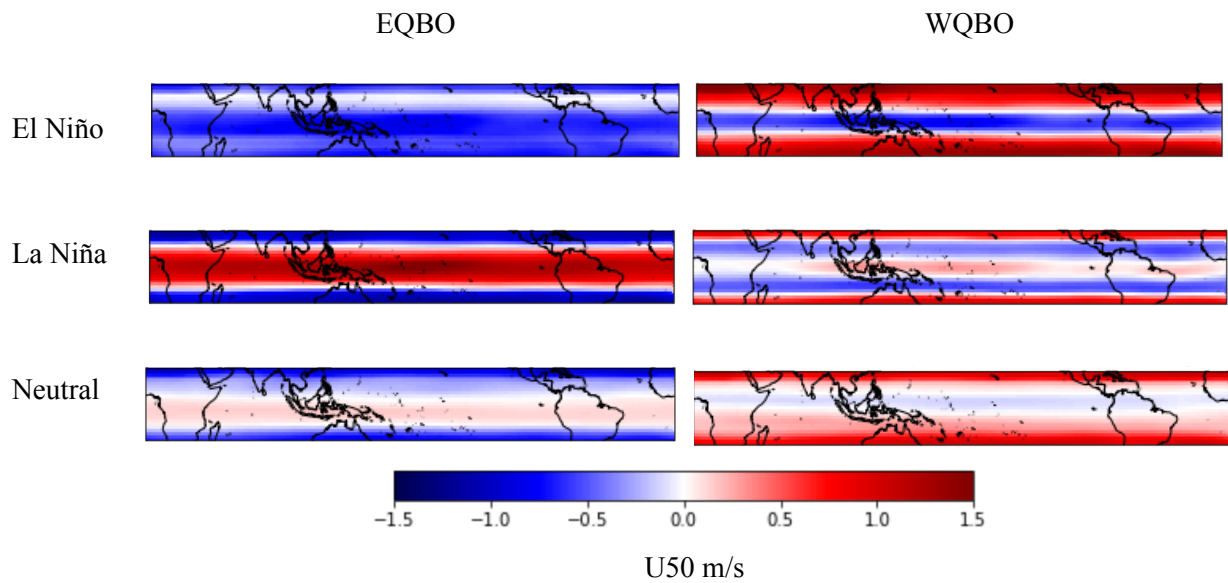

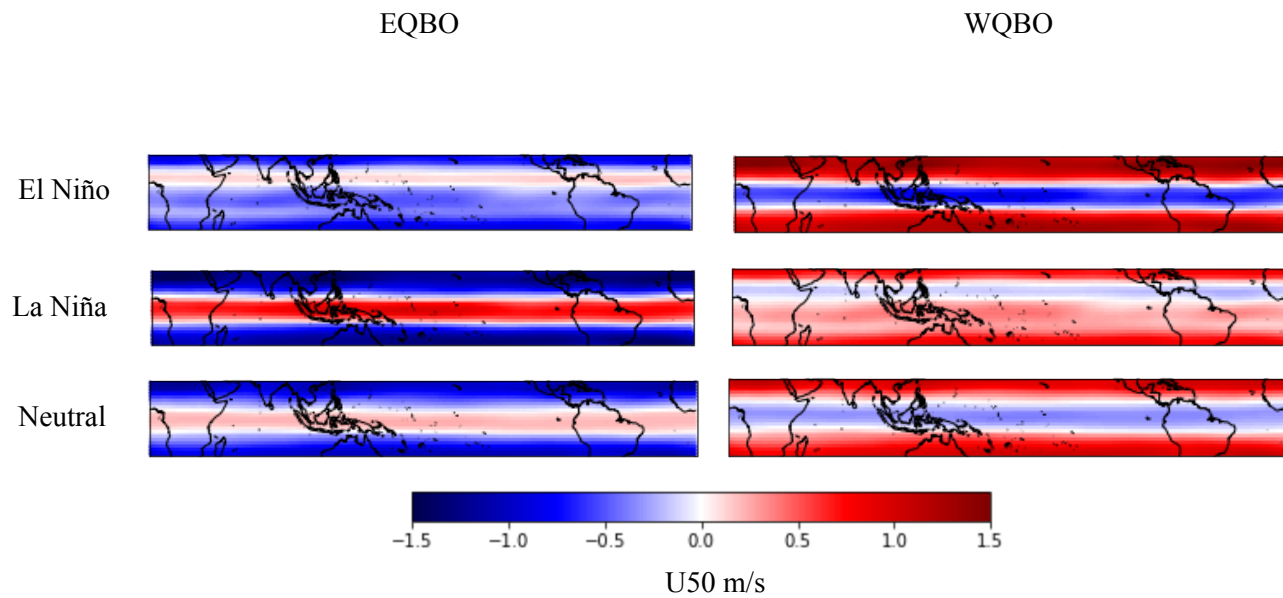−1.5   −1.0   −0.5   0.0   0.5   1.0   1.5

U50 m/s

FIGURE 18: Climate run composite maps of 50-mb zonal wind during El Niño, La Niña, and ENSO neutral events, additionally divided by QBO phase.

Chapter 4

Conclusions & Future Directions

In this study, a linear inverse model is used to analyze connections between the QBO, the MJO, and ENSO. Given that the understanding behind these connections is limited by factors like model performance and the observational record, LIM provides a unique approach. The LIM is derived using anomalous values of SST, Q_1, U_{30_50}, and Ψ. Dynamical filters are used to decompose the data based on the amplitude of the modes for each variable, which coincide with the amount of variance explained. The filtered data is used to create Hovmöller diagrams, which depict patterns throughout space and time during ENSO, QBO, and MJO events. By selecting seasons with specific ENSO phases and strong MJO activity, it's easier to isolate physical processes and assess which signals are having the biggest impact on the full, unfiltered data. The filters additionally allow for examination of interactions between the troposphere and stratosphere. Any relationship between the stratospheric winds, ENSO, and the MJO is captured within the strat-trop-SST subspace.

Forward integration of the LIM provides many more data points based on the statistics from the existing record. Scarcity of data is often an issue when it comes to QBO, MJO, and ENSO analysis, especially given the overlap of their signals. Thus, it becomes useful to look for specific periods where the impact of these phenomena can be removed, shrinking the sample pool even further. Using the extra data points supplied by the forward integration, plots were made to show the power spectra for the first three PCS of each variable in the state vector. By plotting both the full spectra and the power spectra for each filtered subspace, the figures give insight into which subspace contains the most power, and at what frequencies the peaks are located. The power spectra plots for the stratospheric zonal wind also suggest that the variability linked to the zonal wind is at rather low frequencies. For the third PC of zonal wind, most of the power is captured in the strat-trop-sst subspace, indicating that EOF 3 better explains interactions with the troposphere and SST than EOFs 1 and 2 (i.e. the QBO). Additionally, the power spectra plots often depicted power in one of the subspaces exceeding that for the full space. This highlights the non-orthogonality of the filtered spaces, emphasizing the advantages of using linear inverse modeling. The climate run data was also used to create composite maps that could be compared to those from the existing record. From these maps, one can observe differences in each variable throughout different ENSO and QBO phases. For the case of the strat-trop-SST filtered 50-mb zonal wind, there exists some level of asymmetry about the equator in the composites that should be explored more in the future. The composites also suggest forcing from ENSO which affects the stratosphere through anomalous wind values during each QBO phase.

More research is needed to uncover some of the mysteries of these relationships. One possible route is to create different linear inverse models for different time periods, such as before and after the satellite era. This would test any sort of time period dependence within the QBO/MJO/

ENSO relationships, which is likely having an impact. Also, since this study used an ENSO index specific to eastern Pacific ENSO events, it would be interesting to apply other indices, and explore the role that ENSO diversity plays in these connections. Linear inverse modeling can also be utilized to assess how different wave frequencies influence QBO-MJO interactions through an analysis of the noise term. In addition to this, creating extratropical LIMs would give insight into the QBO's impact on MJO teleconnections.

Bibliography

Australian Government Bureau of Meteorology, n.d.: *Madden-Julian Oscillation (MJO)*, Madden-Julian Oscillation (MJO) monitoring. http://www.bom.gov.au/climate/mjo/.

Baldwin, M. P., and Coauthors, 2001: The quasi-biennial oscillation. *Rev. Geophys.*, **39**, 179–229.

Baldwin, M. P., and D. O'Sullivan, 1995: Stratospheric Effects of ENSO-Related Tropospheric Circulation Anomalies. *J. Climate*, **8**, 649–667.

Bjerknes, J., 1966: A possible response of the atmospheric Hadley circulation to equatorial anomalies of ocean temperature. *Tellus A: Dynamic Meteorology and Oceanography*, **18 (4)**, 820-829.

Bjerknes, J., 1969: Atmospheric teleconnections from the equatorial Pacific. *Mon. Wea. Rev.*, **97**, 163–172.

Bond, N. A., and G. A. Vecchi, 2003: The influence of the Madden-Julian Oscillation on precipitation in Oregon and Washington. *Weather Forecasting*, **18**, 600–613.

Bretherton, F. P., 1969: Momentum transport by gravity waves. *Q. J. R. Meteorol. Soc.*, **95**, 213–243.

Bushell, A.C., and Coauthors, 2022: Evaluation of the Quasi-Biennial Oscillation in global climate models for the SPARC QBO-initiative. *Q. J. R. Meteorol. Soc.*, **148**, 1459-1489.

Capotondi, A., and Coauthors, 2015: Understanding ENSO Diversity. *Bull. Amer. Meteor. Soc.*, **96**, 921–938.

Cassou, C., 2008: Intraseasonal interaction between the Madden–Julian Oscillation and the North Atlantic Oscillation. *Nature*, **455**, 523–527.

Deser, C., M. A. Alexander, S.-P. Xie, and A. S. Phillips, 2010: Sea surface temperature variability: patterns and mechanisms. *Annu. Rev. Mar. Sci.* **2**, 115–143.

Ebdon, R. A., 1960: Notes on the wind flow at 50 mb in tropical and subtropical regions in January 1957 and in 1958. *Q. J. R. Meteorol. Soc.*, **86**, 540–542.

Feng, P.-N., and H. Lin, 2019: Modulation of the MJO-related teleconnections by the QBO. *J. Geophys. Res. Atmos.*, **124**, 12022–12033.

Geller, M. A., T. Zhou, and W. Yuan, 2016: The QBO, gravity waves forced by tropical convection, and ENSO. *J. Geophys. Res. Atmos.*, **121**, 8886–8895.

Gray, W. M., J. D. Sheaffer, and J. A. Knaff, 1992: Hypothesized mechanism for stratospheric QBO influence on ENSO variability. *Geophys. Res. Lett.*, **19**, 107–110.

Henderson, S. A., D. J. Vimont, and M. Newman, 2020: The Critical Role of Non-Normality in Partitioning Tropical and Extratropical Contributions to PNA Growth. *J. Climate*, **33**, 6273–6295.

Hendon, H. H., M. C. Wheeler, and C. Zhang, 2007: Seasonal Dependence of the MJO–ENSO Relationship. *J. Climate*, **20**, 531–543.

Hendon, H. H., and S. Abhik, 2018: Differences in vertical structure of the Madden-Julian Oscillation associated with the quasi-biennial oscillation. *Geophys. Res. Lett.*, **45**, 4419–4428.

Hood, L. L., 2017: QBO/solar modulation of the boreal winter Madden-Julian oscillation: A prediction for the coming solar minimum. *Geophys. Res. Lett.*, **44**, 3849–3857.

Kim, Hyemi, J. M. Caron, J. H. Richter, and I. R. Simpson, 2020: The lack of QBO–MJO connection in CMIP6 models. *Geophys. Res. Lett.*, **47**, e2020GL087295.

Kobayashi, S., and Coauthors, 2015: The JRA-55 reanalysis: General specifications and basic characteristics. *J. Meteorol. Soc. Jpn. Ser. II*, **93 (1)**, 5-48.

Krishnamurti, T. N., D. K. Oosterhof, and A. V. Mehta, 1988: Air-sea interaction on the time scale of 30 to 50 days. *J. Atmos. Sci.*, **45**, 1304–1322.

Lau, K.-M., and P. H. Chan, 1986: Aspects of the 40–50 day oscillation during the northern summer as inferred from outgoing longwave radiation. *Mon. Weather Rev.*, **114**, 1354–1367.

Lee, J. C. K., and N. P. Klingaman, 2018: The effect of the quasi-biennial oscillation on the Madden–Julian oscillation in the Met Office Unified Model global ocean mixed layer configuration. *Atmos. Sci. Lett.*, **19**, e816.

L'Heureux, M. L., D. C. Collins, and ZZ. Hu, 2013: Linear trends in sea surface temperature of the tropical Pacific Ocean and implications for the El Niño-Southern Oscillation. *Clim Dyn* **40**, 1223–1236.

L'Heureux, M. L., and R. W. Higgins, 2008: Boreal Winter Links between the Madden–Julian Oscillation and the Arctic Oscillation. *J. Climate*, **21**, 3040–3050.

Liebmann, B., H. Hendon, and J. Glick, 1994: The relationship between tropical cyclones of the western Pacific and Indian oceans and the Madden-Julian Oscillation. *J. Meteorol. Soc. Jpn.*, **72**, 401–411.

Lim, Y., S. Son, A. G. Marshall, H. H. Hendon, and K. Seo, 2019: Influence of the QBO on MJO prediction skill in the subseasonal-to-seasonal prediction models. *Clim Dyn*, **53**, 1681–1695.

Lindzen, R. S., J. R. Holton, 1968: A theory of the quasi-biennial oscillation. *J. Atmos. Sci.*, **25**, 1095–1107.

Lu, J., G. Chen, and D. M. W. Frierson, 2008: Response of the Zonal Mean Atmospheric Circulation to El Niño versus Global Warming. *J. Climate*, **21**, 5835–5851.

Madden, R. A., and P. R. Julian, 1971: Detection of a 40–50 day oscillation in the zonal wind in the tropical Pacific. *J. Atmos. Sci.*, **28**, 702–708.

Madden, R. A., and P. R. Julian, 1972: Description of global-scale circulation cells in the tropics with a 40 − 50 day period. *J. Atmos. Sci.*, **29**, 1109–1123.

Marshall, A. G., H. H. Hendon, S. Son, and Y. Lim, 2017: Impact of the quasi-biennial oscillation on predictability of the Madden–Julian oscillation. *Clim Dyn* **49**, 1365–1377.

Martin, Z., S. Wang, J. Nie, and A. Sobel, 2019: The Impact of the QBO on MJO Convection in Cloud-Resolving Simulations. *J. Atmos. Sci.*, **76**, 669–688.

Maruyama, T., 1997: The quasi-biennial oscillation (QBO) and equatorial waves-A historical review, *Pap. Meteorol. Geophys.*, **48**, 1–17.

Maruyama, T., and Y. Tsuneoka, 1988: Anomalously short duration of easterly wind phase of the QBO at 50 hPa in 1987 and its relationship to an El Niño event. *J. Meteor. Soc. Japan,* **66,** 629–633.

Newman, M., P. D. Sardeshmukh, and C. Penland, 2009: How Important Is Air–Sea Coupling in ENSO and MJO Evolution?. *J. Climate*, **22**, 2958–2977.

Nishimoto, E., and S. Yoden, 2017: Influence of the Stratospheric Quasi-Biennial Oscillation on the Madden–Julian Oscillation during Austral Summer. *J. Atmos. Sci.*, **74**, 1105–1125.

NOAA Physical Sciences Laboratory, n.d.: *TOP 24 STRONGEST EL NIÑO AND LA NIÑA EVENT YEARS BY SEASON*, El Niño Southern Oscillation (ENSO). https://psl.noaa.gov/enso/climaterisks/years/top24enso.html.

Penland, C., 1989: Random forcing and forecasting using principal oscillation pattern analysis. *Mon. Wea. Rev*, **117**, 2165–2185.

Penland, C., and L. Matrosova, 1994: A Balance Condition for Stochastic Numerical Models with Application to the El Niño-Southern Oscillation. *J. Climate*, **7**, 1352–1372.

Penland, C., and L. Matrosova, 2006: Studies of El Niño and Interdecadal Variability in Tropical Sea Surface Temperatures Using a Nonnormal Filter. *J. Climate*, **19**, 5796–5815.

Penland, C., and P. D. Sardeshmukh, 1995: The Optimal Growth of Tropical Sea Surface Temperature Anomalies. *J. Climate*, **8**, 1999–2024.

Philander, S., 1983: El Niño Southern Oscillation phenomena. *Nature*, **302**, 295–301.

Reed, R. J., W. J. Campbell, L. A. Rasmussen, R. G. Rogers, 1961: Evidence of a downward propagating annual wind reversal in the equatorial stratosphere. *J. Geophys. Res.*, **66**, 813–818.

Son, S., Y. Lim, C. Yoo, H. H. Hendon, and J. Kim, 2017: Stratospheric Control of the Madden–Julian Oscillation. *J. Climate*, **30**, 1909–1922.

Suarez, M. J., and P. S. Schopf, 1988: A Delayed Action Oscillator for ENSO. *J. Atmos. Sci.*, **45**, 3283–3287.

Tompkins, A. M., 2001: Organization of tropical convection in low vertical wind shears: The role of water vapor. *J. Atmos. Sci.*, **58**, 529–545.

van Loon, H., and K. Labitzke, 1987: The Southern Oscillation. Part V: The anomalies in the lower stratosphere of the Northern Hemisphere in winter and a comparison with the quasi-biennial oscillation. *Mon. Wea. Rev.*, **115 ,** 357–369.

Wallace, J. M., and F-C. Chang, 1982: Interannual variability of the wintertime polar vortex in the Northern Hemisphere middle atmosphere. *J. Meteor. Soc. Japan*, **60 ,** 149–155.

Wallace, J. M., J. R. Holton, A diagnostic numerical model of the quasi-biennial oscillation, J. Atmos. Sci., 25, 280–292, 1968.

Wallace, J. M., and V. E. Kousky, 1968: Observational Evidence of Kelvin Waves in the Tropical Stratosphere. *J. Atmos. Sci.*, **25**, 900–907.

Wang, J., H. Kim, E. K. M. Chang, and S. Son, 2018: Modulation of the MJO and North Pacific storm track relationship by the QBO. *J. Geophys. Res. Atmos.*, **123**, 3976–3992.

Winkler, C. R., M. Newman, and P. D. Sardeshmukh, 2001: A Linear Model of Wintertime Low-Frequency Variability. Part I: Formulation and Forecast Skill. *J. Climate*, **14**, 4474–4494.

Yang, S., Z. Li, J. Yu, X. Hu, W. Dong, S. He, 2018: El Niño–Southern Oscillation and its impact in the changing climate. *National Science Review*, **5 (6)**, 840–857.

Yu, J., Y. Zou, S. T. Kim, and T. Lee, 2012: The changing impact of El Niño on US winter temperatures. *Geophys. Res. Lett.*, **39**, L15702.

Zhang, C., 2005: Madden-Julian Oscillation. *Rev. Geophys.*, **43**, RG2003.

Zhang, C., and B. Zhang, 2018: QBO-MJO connection. *J. Geophys. Res. Atmos.*, **123**, 2957–2967.